Optics Letters

Two-photon polymerization of microstructures by a non-diffraction multifoci pattern generated from a superposed Bessel beam

Liang Yang,[1] Dongdong Qian,[1] Chen Xin,[1] Zhijiang Hu,[1] Shengyun Ji,[1] Dong Wu,[1,*] Yanlei Hu,[1,2] Jiawen Li,[1] Wenhao Huang,[1] and Jiaru Chu[1]

[1]CAS Key Laboratory of Mechanical Behavior and Design of Materials, Department of Precision Machinery and Precision Instrumentation, University of Science and Technology of China, Hefei 230026, China
[2]e-mail: huyl@ustc.edu.cn
*Corresponding author: dongwu@ustc.edu.cn

Received 13 December 2016; accepted 5 January 2017; posted 17 January 2017 (Doc. ID 282756); published 8 February 2017

In this Letter, superposed Bessel beams (SBBs) are realized by alternatively imprinting holograms of opposite-order Bessel beams along the radial direction on a spatial light modulator. The propagation invariance and non-rotation properties of SBBs are theoretically predicted and experimentally demonstrated. The focusing property of SBBs with a high numerical aperture (NA) objective is investigated with the Debye vectorial diffraction theory. Near the focal plane, a circularly distributed multiple foci pattern is achieved. The multiple foci generated from SBBs are adopted in a two-photon fabrication system, and micropattern fabrication by a single exposure is demonstrated. Facile fabrication of three-dimensional microstructures with SBBs is realized by dynamically controlling the number of focal spots, and the diameter and rotation of the focal pattern.

OCIS codes: (090.1760) Computer holography; (140.3300) Laser beam shaping; (140.3390) Laser materials processing; (220.4000) Microstructure fabrication; (230.6120) Spatial light modulators.

https://doi.org/10.1364/OL.42.000743

The femtosecond two-photon polymerization (TPP) technique, due to its simplicity, down to sub-100 nanometer resolution [1], and intrinsic three-dimensional (3D) processing ability, is widely used for the high-precision fabrication of complex functional 3D micro- and nanodevices [2–4]. A conventional method is to move the focus of a Gaussian beam within materials to build micro- and nanostructures point by point [5]. To improve the micromachining efficiency and flexibility, microlens arrays [6], diffractive optical elements [7], and multibeam interference [8] are introduced for parallel processing. However, the positions of the foci are fixed by the optical design of these optical elements. It is a flexible and efficient method to fabricate complicated microstructures through spatial laser beam shaping by using a spatial light modulator (SLM) [9–12], which provides the possibility of designing beam shapes that are optimized for specific applications. Up to now, many kinds of shaped beams, including a multiple beam spot array [9], spatially shifted vortex beams [10], and double-helix beams [11] have been explored for the rapid fabrication of functional structures.

Bessel beams, among these engineered specific beams, have drawn broad attentions due to their interesting properties such as propagation invariance, "self-healing," and the possession of orbital angular momentum. Bessel beams have been used in the area of optical trapping and manipulation [13], high-aspect-ratio nanochannel drilling [14], silicon and glass processing [15], and surface structuring [16]. It has become clear that the generation of specific Bessel beams can enable the parallel processing, the enhancement of the processing speed and flexibility, and the creation of the specially required focal pattern in microfabrication.

In this Letter, superposed Bessel beams (SBBs) are realized by using a SLM without any other optical elements. In contrast with other SBB generation methods [17,18], the optical system is much simpler, and the parameter controlling of the SBB is much more convenient. The propagation invariance and non-rotation of SBB is demonstrated. The focusing property of a SBB with a high NA objective is theoretically investigated with the Debye vectorial diffraction theory. The focused SBB is used for efficient TPP, and the experiment results confirm that a multifoci pattern can be fabricated by a single exposure. Furthermore, the flexible fabrication of 3D microstructures by dynamically controlling the multifoci pattern is realized. Our novel laser fabrication process enhances the efficiency and flexibility of microfabrication.

Bessel beams have an intensity profile that approximates Bessel functions, and high-order Bessel beams exhibit a non-diffracting dark core on the beam axis. Bessel beams can be generated by a SLM imprinted with holograms [19] that have the transmission function as below:

$$T_n(r,\theta) = \exp(in\theta)\exp(-i2\pi r/r_0), \tag{1}$$

where r and θ are transverse and polar coordinates, r_0 is an adjustable constant parameter, and n denotes the nth-order

Bessel beam. Since the displayer of the SLM is constituted by pixels, we rewrite $r = (i^2 + j^2)^{1/2}d$, where i and j are integers indicating each pixel of the SLM, and d is the pixel pitch. Figures 1(a) and 1(b) show the holograms corresponding to the 3rd- and -3rd-Bessel beams.

The superposition of Bessel beams can be realized by two methods. The first method is simply adding the transmission function of $T_n(r,\theta)$ and $T_{-n}(r,\theta)$. The second method is to imprint the holograms of the $\pm n$th-order Bessel beam alternately along the radial direction, which is chosen in this Letter to ensure that the generated patterns do not rotate as they propagate. The transmission function for superposed $\pm n$th-order Bessel beam is

$$T_{\pm n}(r,\theta) = \exp(-i2\pi r/r_0)\,\exp[i(-1)^{r/\Delta}n\theta]\exp(i\phi). \quad (2)$$

These holograms are composed of concentric rings with continuous azimuthal modulation from 0 to 2π, and Δ is the width of each ring. The factor ϕ determines the rotating angle of the holograms. The handedness of the azimuthal modulation is determined by the radial coordinate r, and every two neighboring rings have opposite modulation directions (handedness). Figure 1(c) is the result superposed by T_3 and T_{-3}.

The optical field of SBBs behind the SLM can be obtained according to Fresnel diffraction integration:

$$U(x,y,z) = \frac{\exp(ikz)}{i\lambda z}\iint_{\mathrm{SLM}} U_0(x_0,y_0)T_{\pm n}(x_0,y_0) \times \exp\left[ik\frac{(x-x_0)^2+(y-y_0)^2}{2z}\right]\mathrm{d}x_0\mathrm{d}y_0, \quad (3)$$

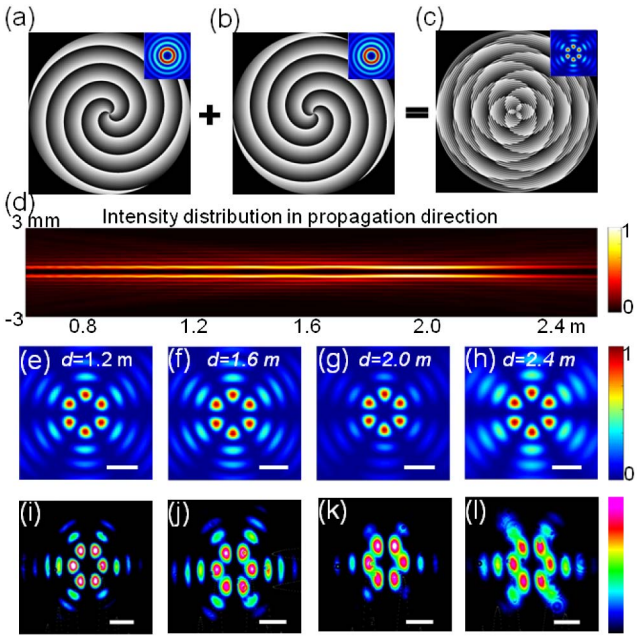

Fig. 1. Generation of SBBs by alternatively imprinting holograms of opposite-order Bessel beams. Hologram of a (a) 3rd-order and (b) -3rd-order Bessel beam. (c) Composite hologram by alternatively imprinting holograms of $\pm$3rd-order Bessel beams. The insets show that the generated beam patterns correspond to the holograms. (d) Calculated intensity distributions along the propagation direction of a SBB generated by imprinting (c) on a SLM. (e)–(h) Calculated intensity distributions in transverse planes at a distance of 1.2, 1.6, 2.0, and 2.4 m, respectively. (i)–(l) Measured intensity distributions corresponding to (e)–(h). The scale bars are 0.5 mm.

where (x, y, z) is the Cartesian coordinate with the origin at the center of the SLM, (x_0, y_0) is the coordinate on the SLM, $U_0(x_0, y_0) = \exp[-(x_0^2 + y_0^2)/w_0^2]$ is the electrical field of the incident laser beam, and w_0 is the waist radius. Theoretical calculation indicates that the intensity profile of a pure Bessel beam is a circular beam pattern [inset of Figs. 1(a) and 1(b)]. For SBBs, a laser beam is divided equally along the circumferential direction, and a petal-like pattern is produced [inset of Fig. 1(c)]. The petal number is decided by the order of SBBs. For a superposition of $n + (-n)$, the final petal number is $2n$. Using the $3 + (-3)$ superposition as an example, generated SBB, as viewed in the far field, is shown in Figs. 1(d)–1(l). Figure 1(d) is the theoretically calculated intensity distribution along the beam propagation direction. The intensity profiles in the transverse direction, at distances of 1.2, 1.6, 2.0, and 2.4 m from the SLM, are also calculated [Figs. 1(e)–1(h)] and experimentally measured [Figs. 1(i)–1(l)]. The theoretical prediction is in excellent agreement with the experimental measurement. It is calculated and observed that the intensity profile remains almost unchanged in a long distance of 2.0 m [Figs. 1(d)–1(l)], which demonstrates the propagation-invariant property of SBBs.

For TPP or other microfabrication processes, the SBBs need to be tightly focused with a high NA objective. The focusing property of SBBs is investigated with the Debye vectorial diffraction theory [9,11]. The field distribution at the focal region is derived according to the Debye vectorial diffraction integral:

$$E_2(x_2,y_2,z_2) = -\frac{iC}{\lambda}\int_0^{\alpha}\int_0^{2\pi}\sin\theta_2\sqrt{\cos\theta_2}P(\theta_2,\varphi_2) \times \exp[ikn_0(z_2\cos\theta_2 + x_2\sin\theta_2\cos\varphi_2 + y_2\sin\theta_2\sin\varphi_2)]\mathrm{d}\theta_2\mathrm{d}\varphi_2, \quad (4)$$

where (x_2, y_2, z_2) is the Cartesian coordinate with the origin at the center of the exit pupil of the objective; C is a constant, λ is 800 nm, the wavelength of incident light; n_0 is 1.518, the refractive index of immersion medium; α is the maximum focusing angle of the objective lens and can be calculated according to the formula $\alpha = \arcsin(\mathrm{NA}/n_0)$; NA is the numerical aperture of the objective lens, and NA = 1.35 in this Letter; θ_2 represents the focusing angle of objective lens, and φ_2 is the azimuthal angle of object plane. $P(\theta_2, \varphi_2)$ indicates the polarization state of the EM field in the focal region. For incidence with linear polarization at X direction, $P(\theta_2, \varphi_2)$ can be rewritten as

$$\boldsymbol{P}(\theta_2,\varphi_2) = [1 + (\cos\theta_2 - 1)\cos^2\varphi_2]\boldsymbol{i} + [(\cos\theta_2 - 1)\cos\varphi_2\sin\varphi_2]\boldsymbol{j} - (\sin\theta_2\cos\varphi_2)\boldsymbol{k}. \quad (5)$$

According to Eqs. (4) and (5), the intensity distributions at the focal region of $3 + (-3)$ [Figs. 2(a) and 2(b)] and $10 + (-10)$ [Figs. 2(c) and 2(d)] SBBs are calculated. The generated intensity distributions at the focal plane are 6 and 20 foci uniformly arranged in a circular manner. The intensity distribution in the XZ direction shows [Figs. 2(b) and 2(d)] that most of laser energy distributes near the focal plane with a depth of focus of 2.8 μm. However, a bit of laser energy distributes about 10 μm above the focal plane. We find that this part of intensity distribution is negligible when $n > 10$. As n decreases, this part of intensity distribution becomes more and more pronounced.

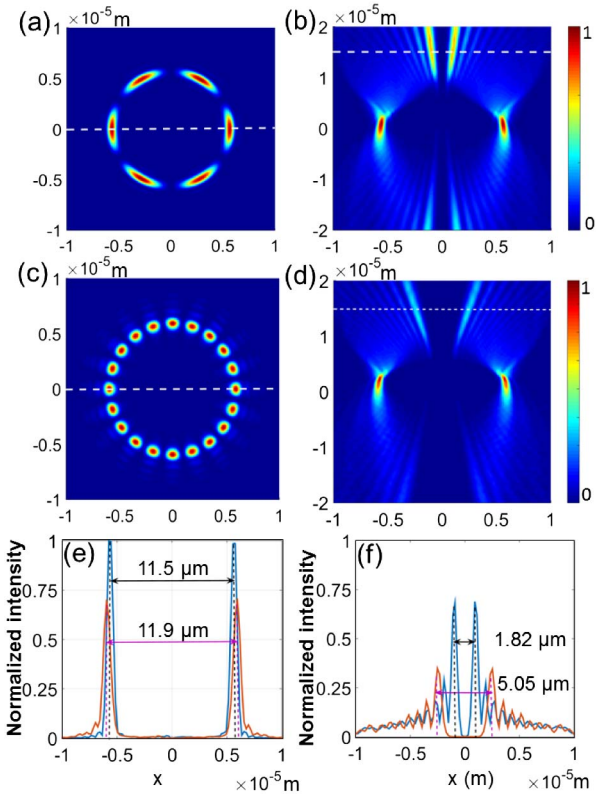

Fig. 2. Intensity distributions of focused SBBs with a high NA objective. (a) and (b) are the intensity distributions at XY and XZ planes of focused 3 + (−3) SBB. (c) and (d) are the intensity distributions of focused 10 + (−10) SBB. (e) and (f) are intensity cross-sectional plots at the focal plane and 15 μm away from the focal plane. The blue line corresponds to the 3 + (−3) SBB, and the brown line corresponds to the 10 + (−10) SBB.

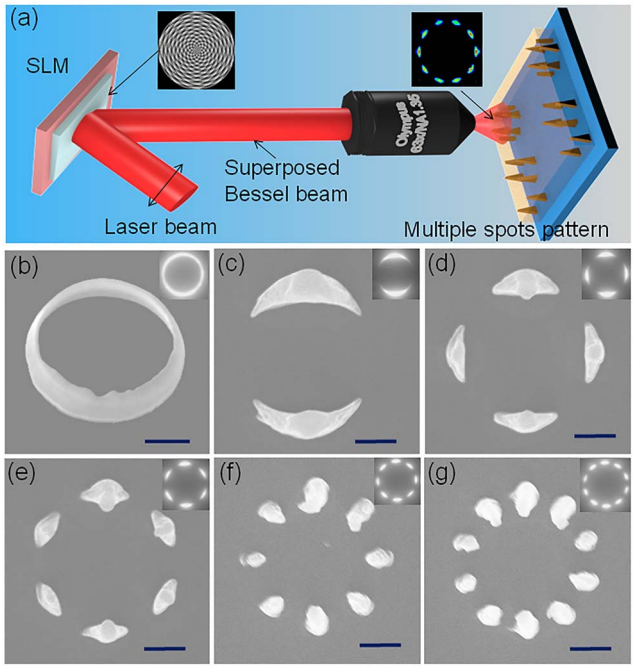

Fig. 3. Single exposure of multiple spot patterns by focused SBBs. (a) Illustration of the microfabrication system. The arrow indicates the polarization direction of the laser beam. The insets are holograms imprinted to a SLM and intensity profile measured at the focal plane of the objective. (b)–(g) SEM images of multispot patterns fabricated by the single exposure of a pure 10th-order Bessel beam, 1 + (−1), 2 + (−2), 3 + (−3), 4 + (−4) and 5 + (−5) SBBs, respectively. The insets are intensity profile captured with a CCD. The scale bars are 3 μm.

The diffraction-limited features of the foci in the focal plane [Fig. 2(e)] and at a location of 15 μm away from the focal plane [Fig. 2(f)] are checked by plotting the intensity distribution along the X direction (marked in a white line). The full widths at half-maximum of the focal spots are 0.44 and 0.54 μm, and the radii of the intensity pattern are 11.5 μm and 11.9 μm, respectively, for 3 + (−3) and 10 + (−10) SBBs. In contrast, the intensity distribution at a location of 15 μm from the focal plane has a lower intensity and a smaller radius.

To experimentally verify the theoretical prediction, a microfabrication system containing phase modulation is implemented, as schematically illustrated in Fig. 3(a). A collimated linearly polarized femtosecond laser beam with a wavelength of 800 nm (Chameleon Ultra, Coherent GmbH) illuminates on an a SLM (Pluto NIR II, Holoeye) with 1920 × 1080 pixels of pitch 8 μm. Calculated holograms (inset) are encoded on the SLM, and generated SBBs are relayed to the back aperture of a high-NA objective lens (60×, NA = 1.35, Olympus). A uniform circular foci pattern is generated at the focal plane of the objective (inset). A multiple spot pattern is prototyped by TPP with a single exposure of photoresist (SZ2080) sample.

Figures 3(b)–3(g) show the scanning electron microscopic (SEM) images of multiple spots fabricated by pure 10th-order Bessel beam, 1 + (−1), 2 + (−2), 3 + (−3), 4 + (−4) and 5 + (−5) SBBs, respectively. The insets are intensity profile observed at the focal plane of objective. All the circular multisport patterns are fabricated by a single exposure, with an exposure time of 100 ms at laser power of 90 mW. The diameters of the circular patterns are ∼11.5 μm, which show exact agreement with the simulation results [Fig. 2(e)]. The fabricated microstructures are symmetrical based on the symmetrical pattern of the superposition of Bessel beams. It should be noted that the laser energy distributes about 10 μm above the focal plane, as illustrated in Figs. 2(b) and 2(d), and two-photon polymerization may arise when the fabrication power exceeds a threshold.

In addition, a remarkable feature of this approach is that the number of focal spots, the diameter, and the rotating angle of the multispot pattern can be flexibly manipulated by controlling the imprinted holograms without any change of the optical path. The number of focal spots is exclusively determined by the order of SBBs, n. The diameter of multiple spot patterns is decided by both the phase factor r_0 and n, according to a theoretical calculation. r_0 plays a dominant role in controlling the diameter, while n affects the diameter slightly. In our experiments, when r_0 varies from 420 to 9600 μm, the diameter of the multispot pattern varies from 12.3 to 0.86 μm and fits well with the theoretical predictions of 12.7 and 1.1 μm. The diameter can be controlled in a much larger range if the limitation of the apertures of the optical elements is eliminated. The rotating angle of the focal pattern is controlled by the factor ϕ.

Flexible control of the optical pattern and fabrication of complicated microstructures is demonstrated based on the dynamical manipulation of SBBs (Fig. 4). We first design

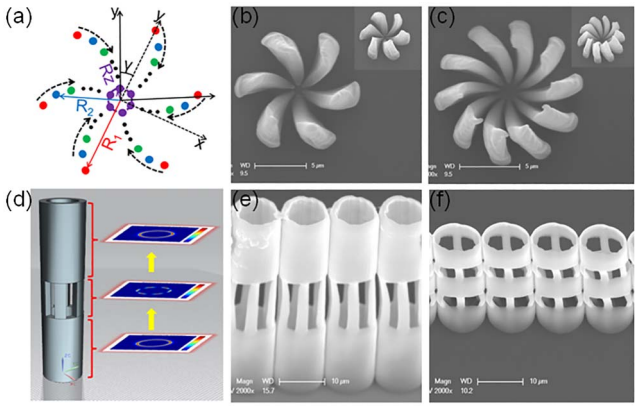

Fig. 4. 3D microstructures fabricated by dynamically controlling the focal pattern. (a) Illustration of the trace of multiple foci for flower-like microstructure fabrication. (b) and (c) are SEM images of flower-like microstructures with six petals and 10 petals, respectively. The scale bars are 5 μm. (d) Illustration of the fabrication process of a microtube with slits. (e) and (f) are SEM images of microtubes with slits. The scale bars are 10 μm.

and generate SBBs by designing the holograms. When the holograms are dynamically switched on the SLM, the generated SBB and its focal pattern composed of multispots will also achieve dynamic motion synchronously. When the diameter and rotating angle of the multifoci pattern change according to a certain rule simultaneously, some special focal trace can be realized. For instance, Fig. 4(a) shows a designed trace composed of six focal spots, of which the diameter decreases from R_1 to R_2 and, finally, to R_z. At the same time, the focal spots rotate clockwise by an angle of γ. Finally, the focal spots move along the black arrow forming a flower-like pattern. In the TPP processing, 52 holograms are dynamically displayed on a SLM with a refresh rate of 10 Hz. The laser power is controlled to be 50 mW. A flower-like microstructure with six petals [Fig. 4(b)] is fabricated. The number of foci can also be controlled [Fig. 4(c)]. When r_0 is changed linearly in Figs. 4(b)–4(c), the diameter of the multifoci decreases faster as the foci close to the center. Thus, the outer side is exposed for a longer period and, finally, exhibits a higher structure than the inner side. Furthermore, by moving the foci pattern along the z direction, together with the dynamic control of the focal pattern, the microtubes with slits, which have important applications in the biomechanical research of cells [20], artificial vasculature [21], physiology study of human spleen [22], and so on, can be rapidly fabricated, as illustrated in Fig. 4(d). When fabricating the microtube parts, pure Bessel beams are generated and, when fabricating the slits parts, a SBB is generated. Figures 4(e) and 4(f) show the SEM image of fabricated microtubes with slits. $3 + (-3)$ superposition is used here, and the diameters of the microtubes are ~12 μm.

In conclusion, we present and demonstrate a method for flexible fabrication of complicated microstructures based on the dynamical control of SBBs through the switching of holograms imprinted on a SLM according to certain rules. First, SBBs are simply realized by alternatively imprinting holograms of $\pm n$-th-order Bessel beams along the radial direction. The generated SBBs propagate invariantly in a long distance of 2.6 m without rotation. Then, we have been able to create micropatterns with a single exposure of focused SBBs. By delicately designing the trace of multiple focal spots and dynamically controlling the imprinted holograms, the number of focal spots, and the diameter and rotation of the focal pattern are well controlled. Finally, on this basis, flexible fabrication of flowerlike microstructures and microtubes with slits are realized. The novel method developed in this Letter deepens the research into the flexible and fast TPP fabrication technique, and the fabricated microtubes with slits are suitable for the number of important applications, such as artificial blood vessels and biomechanical research of blood cells.

Funding. National Natural Science Foundation of China (NSFC) (51675503, 61475149, 51405464, 61675190, 51605463); Fundamental Research Funds for the Central Universities (WK2480000002); China Postdoctoral Science Foundation (2016M590578, 2016M602027); Chinese Academy of Sciences Instrument Project (YZ201566); China Thousand Young Talents Program.

REFERENCES

1. J. Fischer and M. Wegener, Laser Photon. Rev. **7**, 22 (2013).
2. D. Wu, Q. D. Chen, L. G. Niu, J. N. Wang, J. Wang, R. Wang, H. Xia, and H. B. Sun, Lab Chip **9**, 2391 (2009).
3. W. S. Yan, M. M. Hossain, and M. Gu, Opt. Lett. **38**, 3177 (2013).
4. X. Y. Zheng, H. Lee, T. H. Weisgraber, M. Shusteff, J. DeOtte, E. B. Duoss, J. D. Kuntz, M. M. Biener, Q. Ge, J. A. Jackson, S. O. Kucheyev, N. X. Fang, and C. M. Spadaccini, Science **344**, 1373 (2014).
5. T. C. Chong, M. H. Hong, and L. P. Shi, Laser Photon. Rev. **4**, 123 (2010).
6. J. Kato, N. Takeyasu, Y. Adachi, H. B. Sun, and S. Kawata, Appl. Phys. Lett. **86**, 044102 (2005).
7. X. Z. Dong, Z. S. Zhao, and X. M. Duan, Appl. Phys. Lett. **91**, 124103 (2007).
8. X. Jia, T. Q. Jia, L. E. Ding, P. X. Xiong, L. Deng, Z. R. Sun, Z. G. Wang, J. R. Qiu, and Z. Z. Xu, Opt. Lett. **34**, 788 (2009).
9. L. Yang, A. El-Tamer, U. Hinze, J. W. Li, Y. L. Hu, W. H. Huang, J. R. Chu, and B. N. Chichkoy, Opt. Lasers Eng. **70**, 26 (2015).
10. H. Lin and M. Gu, Appl. Phys. Lett. **102**, 084103 (2013).
11. S. J. Zhang, Y. Li, Z. P. Liu, J. L. Ren, Y. F. Xiao, H. Yang, and Q. H. Gong, Appl. Phys. Lett. **105**, 061101 (2014).
12. A. Wang, L. Jiang, X. Li, Y. Liu, X. Dong, L. Qu, X. Duan, and Y. Lu, Adv. Mater. **27**, 6238 (2015).
13. E. McLeod and C. B. Arnold, Opt. Express **17**, 3640 (2009).
14. M. K. Bhuyan, P. K. Velpula, J. P. Colombier, T. Olivier, N. Faure, and R. Stoian, Appl. Phys. Lett. **104**, 021107 (2014).
15. C. Mauclair, A. Mermillod-Blondin, S. Landon, N. Huot, A. Rosenfeld, I. V. Hertel, E. Audouard, I. Myiamoto, and R. Stoian, Opt. Lett. **36**, 325 (2011).
16. X. M. Yu, C. A. Trallero-Herrero, and S. T. Lei, Appl. Surf. Sci. **360**, 833 (2016).
17. R. Vasilyeu, A. Dudley, N. Khilo, and A. Forbes, Opt. Express **17**, 23389 (2009).
18. N. Barbieri, M. Weidman, G. Katona, M. Baudelet, Z. Roth, E. Johnson, G. Siviloglou, D. Christodoulides, and M. Richardson, J. Opt. Soc. Am. A **28**, 1462 (2011).
19. J. A. Davis, E. Carcole, and D. M. Cottrell, Appl. Opt. **35**, 593 (1996).
20. W. Xi, C. K. Schmidt, S. Sanchez, D. H. Gracias, R. E. Carazo-Salas, S. P. Jackson, and O. G. Schmidt, Nano Lett. **14**, 4197 (2014).
21. B. Y. Zhang, M. Montgomery, M. D. Chamberlain, S. Ogawa, A. Korolj, A. Pahnke, L. A. Wells, S. Masse, J. Kim, L. Reis, A. Momen, S. S. Nunes, A. R. Wheeler, K. Nanthakumar, G. Keller, M. V. Sefton, and M. Radisic, Nat. Mater. **15**, 669 (2016).
22. I. V. Pivkin, Z. L. Peng, G. E. Karniadakis, P. A. Buffet, M. Dao, and S. Suresh, Proc. Natl. Acad. Sci. USA **113**, 7804 (2016).